SAND2018-10097J

Optimal design of a model energy conversion device

Lincoln Collins[1] and Kaushik Bhattacharya*[2]

[1] Sandia National Laboratories, Albuquerque NM 87185
[2]California Institute of Technology, Pasadena CA 91125

August 7, 2018

Abstract

Fuel cells, batteries, thermochemical and other energy conversion devices involve the transport of a number of (electro-)chemical species through distinct materials so that they can meet and react at specified multi-material interfaces. Therefore, morphology or arrangement of these different materials can be critical in the performance of an energy conversion device. In this paper, we study a model problem motivated by a solar-driven thermochemical conversion device that splits water into hydrogen and oxygen. We formulate the problem as a system of coupled multi-material reaction-diffusion equations where each species diffuses selectively through a given material and where the reaction occurs at multi-material interfaces. We introduce a phase-field formulation of the optimal design problem, and numerically study selected examples.

1 Introduction

The efficiency of fuel cells, batteries and thermochemical energy conversion devices depends on inherent material characteristics that govern the complex chemistry and transport of multiple species as well as the spatial arrangement of the various materials. Therefore, optimization of the spatial arrangement is a recurrent theme in energy conversion devices. Traditional methods of synthesis offer limited control of the microstructure and there has been much work in advanced imaging for these uncontrolled microstructures (e.g., [31]) and optimizing gross features. However, the growing ability for directed synthesis [28, 21, 29, 23] allows us to ask the question of what microgeometries are optimal for particular applications. In this sense we direct the problem to one of optimal design where we are not limited by the imagination in determining new microstructures but instead allow for the underlying physical behavior and optimization techniques to direct architecture and microstructure, and eventually lead synthesis to unprecedented performance.

The tailoring of material microstructure and nanostructure is not new to energy conversion and storage [23, 4]. The development of hierarchical structures and porosity affords balancing interfacial reactions and chemical transport to maximize efficiency. For example, in cathodes of solid oxide fuel cells, the efficiency is largely determined by reactions at triple phase boundaries and the availability of transport pathways through each phase. These features are coupled with volume fractions, surface area densities, interfacial curvatures, and phase tortuosities to find the optimal balance between surface reaction and transport [30, 25]. Similarly, the importance of microstructure on anode performance [5, 27, 15, 12] has also been established. The morphology of materials used in

*Corresponding Author: bhatta@caltech.edu

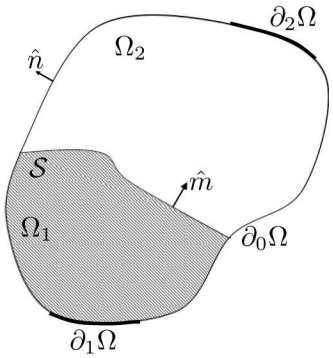

Figure 1: The physical setting: chemical species 1 enters through the source $\partial_1\Omega$, diffuses through Ω_1, is converted to chemical species 2 through a surface reaction at the interface $\mathcal{S}$, chemical species 2 diffuses through Ω_2 and leaves through the sink $\partial_2\Omega$.

lithium ion batteries is of interest from both the theoretical [26, 10, 9] and experimental standpoint [19, 20, 29]. Mass and ion transport and interface measure in battery electrodes directly impact the storage capacity and rate performance and is an ideal problem for optimization across many length scales.

In this paper, we are interested in the problem shown in Figure 1. Chemical species 1 enters through the source $\partial_1\Omega$, diffuses through Ω_1, is converted to chemical species 2 through a surface reaction at the interface $\mathcal{S}$, chemical species 2 diffuses through Ω_2 and leaves through the sink $\partial_2\Omega$. Given the overall domain Ω, the inlet $\partial_1\Omega$, the outlet $\partial_2\Omega$ as well as the concentration of the species at the inlet and the outlet, we seek to find the best arrangement of the two domains Ω_1, Ω_2 separated by the interface $\mathcal{S}$ to maximize the flux through the system.

This problem is motivated by metal oxides in solar-driven thermochemical conversion devices. The application of metal oxides for solar-driven thermochemical conversion devices offers a promising new sustainable energy source [11]. The lack of complex and expensive catalyst systems and full use of the entire solar spectrum separate these devices from many other photo-based energy sources. Here, a porous, redox active oxide is cyclically exposed to inert gas at high temperature, generating oxygen vacancies in the structure, and reactant gas (H_2O, CO_2), at moderate temperature, releasing fuel upon reoxidation the oxide [28]. We have a two phase material (solid oxide and pore) where reactions at the surface create (gaseous) oxygen in the carrier gas in the pores and bound oxygen in the solid oxide; the oxygen diffuses through the carrier gas in the porous region and bound oxygen diffuses through the solid oxide. We seek to understand the arrangement of the solid and porous regions to maximize the transport given sources and sinks for the gaseous oxygen and vacancies. We note that there are a number of other areas of energy conversion devices that lead to similar problems.

There is a large literature in the study of optimal design problems, especially seeking to minimize compliance for a given weight as well as maximize conduction for a given mass. It is understood that the underlying problem is ill-posed in that the optimal designs often lie outside of the set of "classical admissible designs." One has to either relax the problem by homogenization [18, 22] or regularize it through the introduction of constraints: e.g. on the perimeter [3, 8], on the geometry itself via a curvature bound, or fixing the topology of the material domain a-priori [24]. These treatments lead to a variety of widely used methods in shape and topology optimization [6, 1]. The presence of two species lends a vectorial character to our problem, and the presence of the surface sources makes the problem at hand different from those in the literature.

We formulate our optimization problem in Section 2. We begin with a sharp interface formulation of physical problem in Section 2.1. However, the optimal design of the sharp interface model is difficult. Therefore we introduce a diffuse interface model by adding a Allen-Cahn term to describe the phase arrangement in Section 2.2. We solve this numerically in selected examples in Section 3 and conduct a parameter study. These show that the optimal design can be quite intricate as it seeks to balance transport and reaction.

2 Formulation

2.1 Sharp interface formulation

Consider an open, bounded region $\Omega \subset \mathbb{R}^n$ with Lipschitz boundary separated into two regions Ω_1 and Ω_2 by an interface $\mathcal{S}$ as shown in Figure 1. We consider the diffusion of one species with concentration u_1 in region Ω_1 with isotropic diffusivity $K_1 > 0$, and a second species with concentration u_2 in region Ω_2 with isotropic diffusivity $K_2 > 0$. The two species meet at the interface and react with reaction rate $k_s > 0$. The boundary of Ω is divided into three regions $\partial\Omega = \partial_1\Omega \cup \partial_2\Omega \cup \partial_0\Omega$ where $\partial_i\Omega \subset \partial\Omega_i$. The concentration of species i is held at a prescribed value u_i^* on $\partial_i\Omega$ while $\partial_0\Omega$ is insulating. This is described by the following system of equations:

$$\begin{cases} \nabla \cdot K_i \nabla u_i = 0 & \text{in } \Omega_i \\ -K_i \nabla u_i \cdot \hat{m} = k_s(u_1 - u_2) & \text{on } \mathcal{S} \\ u_i = u_i^* & \text{on } \partial_i\Omega \\ K_i \nabla u_i \cdot \hat{n} = 0 & \text{on } \partial\Omega \setminus \partial_i\Omega \end{cases} \tag{1}$$

for $i = 1, 2$ where $\hat{m}$ represents the normal to $\mathcal{S}$ pointing from Ω_1 pointing to Ω_2, and $\hat{n}$ represents the outward normal to $\partial\Omega$. The first equations describes the diffusion of the ith species in Ω_i while the second describes the reaction kinetics and mass balance at the interface $\mathcal{S}$. Finally, the third and the fourth condition describe the boundary conditions.

It is easy to see that the problem above is the same as minimizing

$$L(u, \chi) = \int_\Omega \left(\chi \frac{K_1}{2} |\nabla u_1|^2 + (1 - \chi) \frac{K_2}{2} |\nabla u_2|^2 \right) dx + \int_S \frac{k_s}{2} (u_1 - u_2)^2 dA \tag{2}$$

over u_1, u_2 subject to $(1)_3$ where χ is the characteristic function of Ω_1.

We seek the arrangement of two subregions Ω_1 and Ω_2 that maximizes the flux through the domain:

$$\int_{\partial_1\Omega} K_1 \nabla u_1 \cdot n dA = -\int_{\partial_2\Omega} K_2 \nabla u_2 \cdot n dA$$

where n is the outward normal to Ω, u_1, u_2 solve (1) and the equality follows from (1). In practice, it is common to have u_i^* uniform over $\partial_i\Omega$. So, by normalizing if necessary, we take objective function to be

$$\mathcal{O} = \frac{1}{2} \int_{\partial_1\Omega} u_1 K_1 \nabla u_1 \cdot n dA - \frac{1}{2} \int_{\partial_2\Omega} u_2 K_2 \nabla u_2 \cdot n dA.$$

We can use (1) to show that $L = \mathcal{O}$. Thus, we study the optimization problem

$$\max_{\chi} \min_{u_1, u_2} L(u, \chi) \tag{3}$$

subject to a constraint on the volume fraction v of Ω_1.

2.2 Diffuse interface formulation

The optimization problem above is difficult to solve directly. So, we regularize it with a diffuse interface formulation. The idea is to introduce a smooth function χ that approximates the characteristic function of Ω_1. Recall the Allen-Cahn functional [2]

$$\int_\Omega \left(\alpha W(\chi) + \beta|\nabla\chi|^2\right)\, dx,$$

for

$$W(\chi) = \chi^2(1-\chi)^2.$$

The minimizers of this functional are smooth and take values close to 0 and 1 separated by regions of thickness of the order of $\sqrt{\beta/\alpha} \to 0$. Indeed, near the boundaries between the sets, the minimizers are of the form

$$\chi(\xi) = \frac{1}{2}\left(\tanh\left(\sqrt{\frac{\alpha}{\beta}}\xi\right) + 1\right)$$

where ξ is the coordinate normal to the boundary. Thus, minimizers of the Allen-Cahn functional approach the characteristic function of sets in the limit $\sqrt{\beta/\alpha} \to 0$.

Therefore, we consider the functional

$$\mathcal{L}(u,\chi) = \int_\Omega \left(\frac{1}{2}\sum_{i=1,2} k_i|\nabla u_i|^2 + \frac{k_s}{2c}\chi(1-\chi)(u_1-u_2)^2 - \lambda\chi - \left(\alpha W(\chi) + \beta|\nabla\chi|^2\right)\right) dx, \tag{4}$$

where

$$k_1(x) = k_{11}\chi(x) + k_{12}(1-\chi(x)), \quad k_2(x) = k_{21}\chi(x) + k_{22}(1-\chi(x)) \tag{5}$$

with $k_{11} = K_1, k_{22} = K_2 >> k_{12}, k_{21} > 0$ and c is a constant of order unity dependent on the choices of α, β, and study the optimization problem

$$\max_{\chi} \min_{u_1,u_2} \mathcal{L}(u,\chi). \tag{6}$$

Henceforth, we take $c = 1$ redefining k_s as appropriate.

Notice that we have extended the definition of u_1, u_2 to the entire domain, but taken the diffusivity of species 1 in region 2 and species 2 in region 1 to be extremely small. The second term in the integrand of (4) approximates the interfacial term of (2). For any χ that approximates a characteristic function, the product $\chi(1-\chi)$ is almost zero everywhere except near the interface. λ is a Lagrange multiplier that enforces the constraint on the volume fraction of region 1. The final two terms are the Allen-Cahn functional that forces χ to approximate a characteristic function.

Note that given any $\chi \in H^1(\Omega,[0,1])$, $\mathcal{L}(u,\chi)$ is strictly convex in u. So it follows (see for example Dacorogna [16]) that there exists a unique minimizer $u_\chi \in \{u \in H^1(\Omega,\mathbb{R}^2), u_i = u_i^* \text{ on } \partial_i\Omega\}$. Now define

$$\mathcal{F}(\chi) = \mathcal{L}(u_\chi,\chi) = \min_u \mathcal{L}(u,\chi).$$

Let $\{\chi_k\}$ be a maximizing sequence for $\mathcal{F}$. It is easy to show that $\{\chi_k\}$ is bounded in $H^1 \cap L^\infty$. It follows that there is a subsequence (suitably relabelled) and χ_0 such that $\chi_k \rightharpoonup \chi_0$ in H^1 and $\chi_k \overset{*}{\rightharpoonup} \chi_0$ in L^∞, where $\rightharpoonup$ and $\overset{*}{\rightharpoonup}$ denote weak convergence and weak $*$convergence, respectively. Now,

$$\begin{aligned}
\limsup_{k\to\infty} \mathcal{F}(\chi_k) - \mathcal{F}(\chi_0) &= \limsup_{k\to\infty} \left(\mathcal{L}(u_{\chi_k},\chi_k) - \mathcal{L}(u_{\chi_0},\chi_0)\right) \\
&\le \limsup_{k\to\infty} \left(\mathcal{L}(u_{\chi_k},\chi_k) - \mathcal{L}(u_{\chi_0},\chi_k)\right) + \limsup_{k\to\infty} \left(\mathcal{L}(u_{\chi_0},\chi_k) - \mathcal{L}(u_{\chi_0},\chi_0)\right) \\
&\le 0.
\end{aligned}$$

Note that the term in the first parenthesis is non-positive since u_{χ_k} is a minimizer of $\mathcal{L}(u, \chi_k)$. Since the sequence χ_k is (strongly) compact in any L^p with $1 \leq p < +\infty$ from Sobolev embedding, for any fixed u, $\mathcal{L}(u, \chi)$ is upper-semicontinuous in χ. Thus, the second limsup is non-positive. It follows that χ_0 maximizes $\mathcal{F}$, and thus the min-max problem (6) is well-posed.

3 Numerical study of the optimal design problem

We seek to find the solution to our optimal design problem (6) by considering a gradient flow:

$$\int_\Omega \frac{\partial \chi}{\partial t} \varphi \, dx = \frac{1}{d_\chi} \langle \delta_\chi \mathcal{L}, \varphi \rangle$$
$$\int_\Omega \frac{\partial u}{\partial t} \psi \, dx = -\frac{1}{d_u} \langle \delta_u \mathcal{L}, \psi \rangle$$

for every $\varphi, \psi \in H^1(\Omega; \mathbb{R}^N)$ subject to the appropriate boundary conditions. Here $\langle \cdot \rangle$ denotes the L^2 inner product, $\delta_\chi \mathcal{L}$ and $\delta_u \mathcal{L}$ denote the first variations of $\mathcal{L}$ with respect to χ and u, and $d_\chi, d_u > 0$ are the inverse mobilities. We obtain the following system of equations:

$$d_\chi \frac{\partial \chi}{\partial t} = \sum_{i=1,2} \frac{k_i'}{2} |\nabla u_i|^2 + \frac{1}{2} u \cdot Au(1 - 2\chi) - \lambda + \beta \nabla^2 \chi - \alpha W'(\chi), \tag{7}$$

$$d_u \frac{\partial u_i}{\partial t} = \nabla \cdot k_i \nabla u_i - \chi(1 - \chi) A_{ij} u_j \tag{8}$$

subject to boundary conditions and constraints, with

$$A = k_s \begin{pmatrix} 1 & -1 \\ -1 & 1 \end{pmatrix}.$$

We have implemented the system of equations (7), (8) using the commercial software COMSOL [14]. All our simulations are in two dimensions ($n = 2$). We work with non-dimensional units where the size of the domain, the concentration at a boundary and the (diagonal components of the) diffusion coefficient are $\mathcal{O}(1)$. We discretize the problem spatially using linear finite elements generated by Delaunay triangulation, and integrate the resulting ordinary differential equation in time by using the backward differentiation formula. We impose the volume fraction of region 1, v, as a global constraint that is built into COMSOL, removing the need to calculate λ for each iteration. Additionally, we impose a point-wise constraint restricting $\chi \in [0, 1]$. We typically begin with an initial guess of uniform χ, and run the simulations until an apparent steady state is reached (i.e., when the right hand sides of (7) and (8) become small compared to a given tolerance). The simulations can get stuck in local optima, but we try to avoid this by doing parameter sweeps and studying additional initial conditions. Variations in the inverse mobilities d_χ and d_u are used to balance numerical stability and convergence rate but generally have no impact on the resulting geometries.

3.1 Square reactor

We begin with a square domain, $\Omega = (0, 1)^2$, shown in Figure 2(a). We prescribe $u_1 = 1$ on the left face $\partial_1 \Omega = \{0\} \times (0, 1)$ corresponding to a source of species 1, $u_2 = 0$ on the right face $\partial_2 \Omega = \{1\} \times (0, 1)$ corresponding to a sink of species 2, and zero-flux boundary conditions otherwise. We also impose a zero flux boundary condition on our phase-field variable χ.

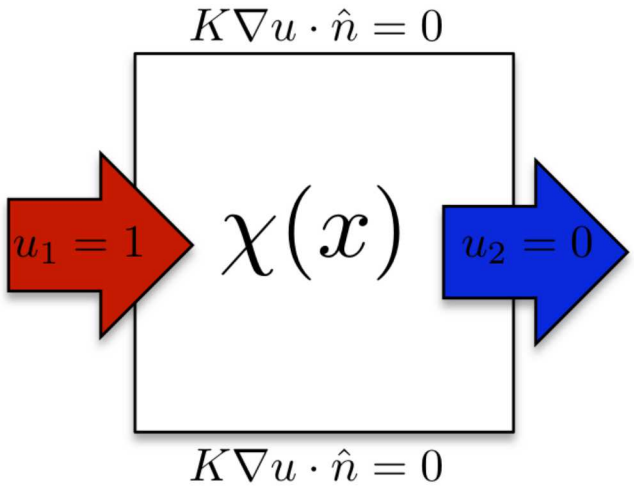

(a)

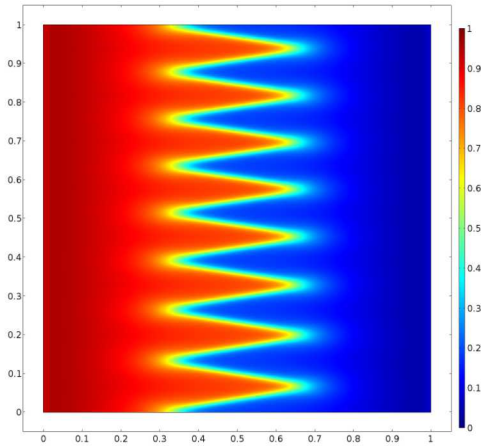

(b)

Figure 2: (a) Square reactor with a source of species 1 on the left and a sink of species 2 on the right. (b) Optimal design (χ) for the parameters in (9)).

The resulting optimal design χ is shown in Figure 2(b) for the parameters

$$\begin{gathered} k_{11} = k_{22} = 1, k_{12} = k_{21} = 1 \times 10^{-6}, k_s = 1 \times 10^2, \\ \alpha = 1, \beta = 2 \times 10^{-5}, \\ v = 0.5. \end{gathered} \tag{9}$$

This simulation had a mesh with 67068 elements, took 845 time steps and the L^2 norm of the time derivative of χ is 3.945×10^{-4} at the end of the simulation. We have verified that the design does not change by refining the mesh and driving the L^2 norm of the time derivative of χ to 10^{-12}. As noted above, the parameters d_χ and d_u which is a rescaling of the time step do not affect the final (stationary) solution and are used to balance numerical stability and convergence rate.

The resulting design has a clear intuitive explanation. Given the boundary conditions, the design seeks to draw in species 1 from the left, react it in the center to convert species 1 to species 2, and expel species 2 at the right. Therefore, the design puts material 1, which has a high diffusivity of species 1, on the left so that it can easily transport species 1 from the source to the interface where the reaction consumes it. Material 2, which has a high diffusivity of species 2, is placed on the right so that it can easily transport species 2 from the interface, where the reaction generates it, to the sink. The design maximizes the reaction by creating a zig-zag interface between the two materials.

We now begin a parameter study for the same problem. Figure 3 shows the resulting designs for a volume fraction $v = 0.5$ for various diffusivities k_{11}, k_{22}. Figures 4 and 5 show the corresponding concentration fields u_1 and u_2 respectively while Figure 6 shows the corresponding reactions by plotting the local evaluation of the second term in the right hand side of $(8)_1$.

We begin at the center for the case $k_{11} = k_{22} = 1$, which is what we described earlier. Decreasing both diffusivities by moving up on the diagonal to $k_{11} = k_{22} = 0.1$ leads to a similar segregation of the material but the interface is sharper and straight. The interfacial reaction constant is now high compared to the diffusion and thus there is no need to increase interfacial reaction by making a zig-zag interface. Further, a straight interface leads to a constant gradient and thus maximizes

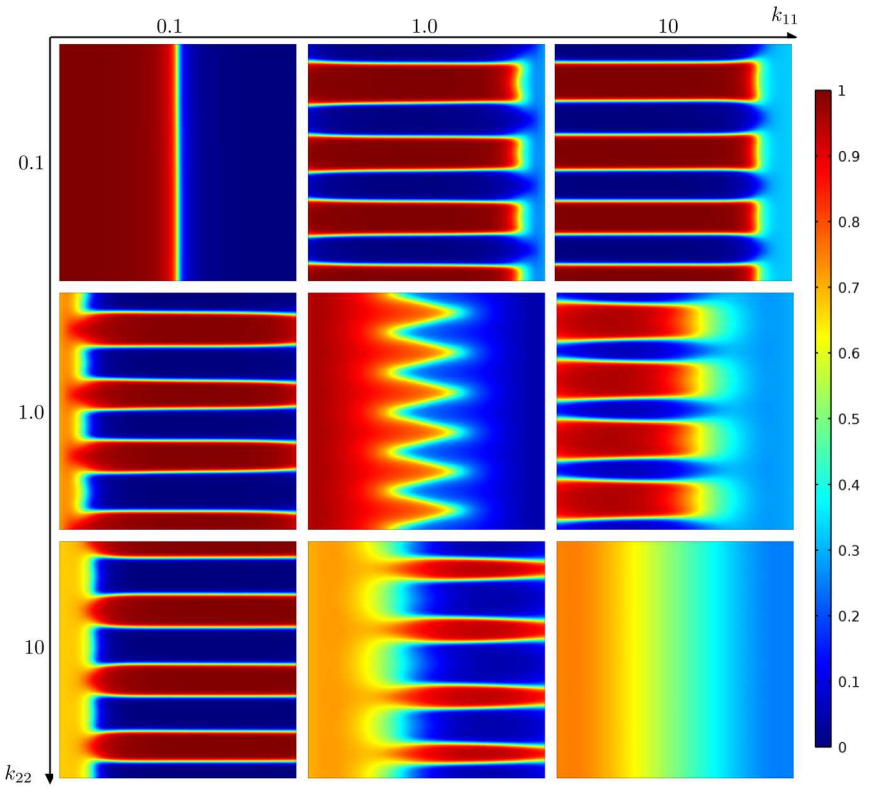

Figure 3: Designs with volume fraction $v = 0.5$ as we vary diffusion coefficients with $\alpha = 0.1$, $\beta = 5 \times 10^{-5}$, $k_{12} = 10^{-3} \times k_{11}$, $k_{21} = 10^{-3} \times k_{22}$, $k_s = 1 \times 10^2$.

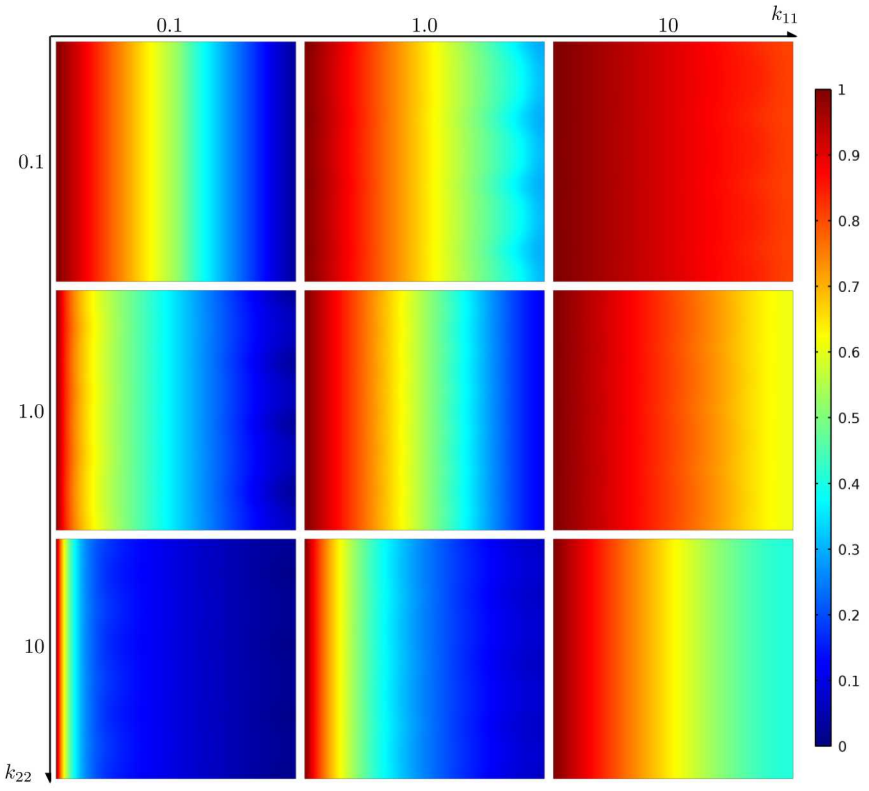

Figure 4: Concentration field u_1 associated with the designs presented in Figure 3.

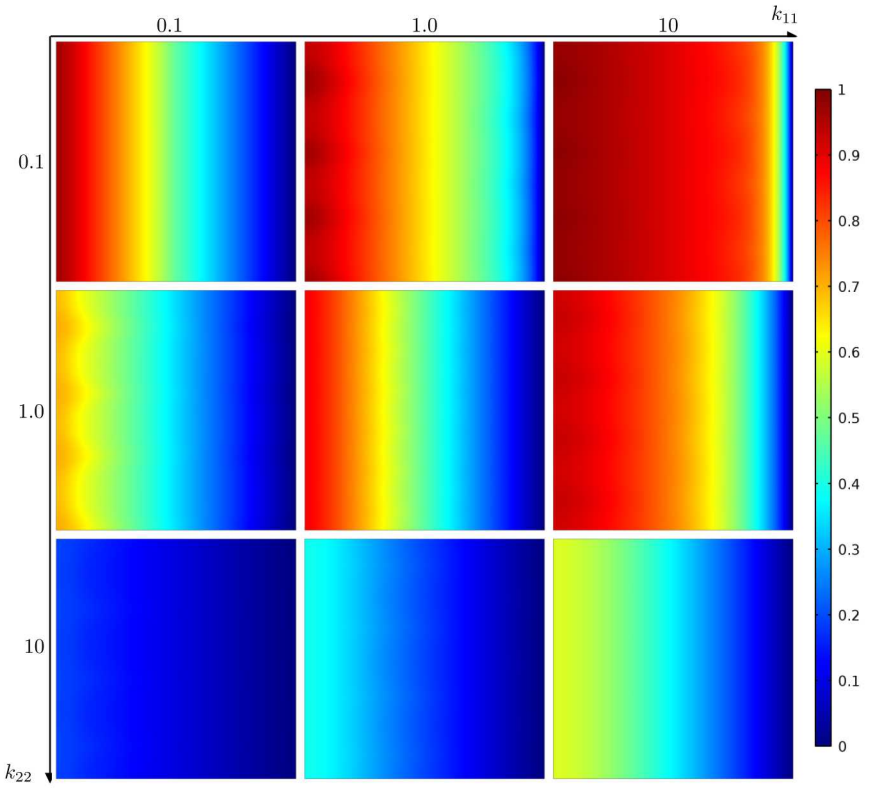

Figure 5: Concentration field u_2 associated with the designs presented in Figure 3.

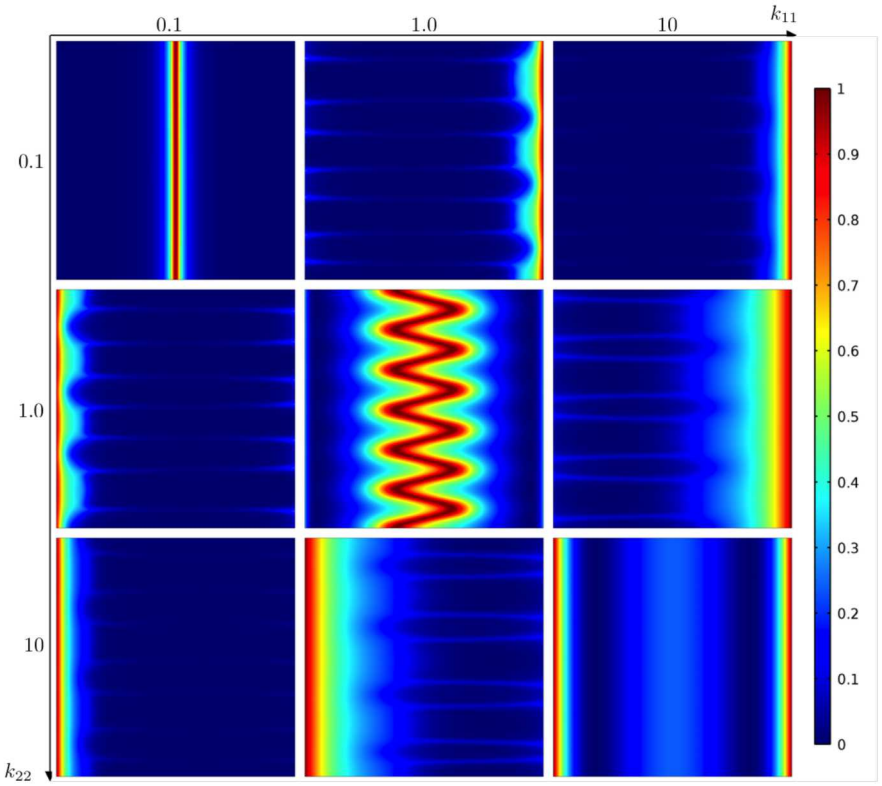

Figure 6: Distribution of reaction (i.e., the right hand side of $(8)_1$) associated with the designs presented in Figure 3; normalized units.

bulk diffusion. We also notice that interface appears sharper despite the fact that the phase field parameters α and β and in particular the ratio β/α remains the same. This is because the decrease of the diffusion constant increases the relative contribution of the phase field part of the energy thereby discouraging mixed material.

On the other hand, increasing both diffusivities by moving down the diagonal to $k_{11} = k_{22} = 10$ still segregates the material, but in a very diffuse manner with an almost constant gradient. Since the diffusivities are both large, the reaction is relatively difficult and diffusion easy. Thus, one would seek to create a highly oscillatory interface with very fine microstructure in a sharp interface model. However, the increased diffusivity also decreases the relative contribution of the phase field energy since α and β are held constant. Therefore, the penalty against mixed material is weakened resulting in a diffuse interface. As we shall see in the next example, increasing α while keeping the ratio β/α fixed enforces pure phases and resolves the diffuse region into an oscillatory interface[1]. In other words, this diffuse interface is an indication of fine-scale structure.

We now turn to the situation when the diffusivities are different. Consider the case when $k_{11} = 1, k_{22} = 0.1$ as shown on the top-center. The diffusion of species 1 is considerably easier than that of species 2. Therefore, it is advantageous to have the reaction close to the sink. Species 1 is transported by the long arms of material 1 (red) which protrude from the left to the right where it reacts very close to the sink, thereby reducing the distance that species 2 has to be transported. The excess material 2 (blue) is 'hidden' on the left in arms that do not participate in the transport. The case $k_{11} = 10, k_{22} = 0.1$ shown on the top-right is similar with a slightly wider interface since reaction is more difficult compared to the transport. The seemingly constant concentration field for u_1 in this case is a consequence of the normalization across all the cases, but exhibits similar structure to the previous case mentioned. The surplus of this species also propagates into the non-favorable phase because of the non-zero diffusivity k_{12}. The case $k_{11} = 10, k_{22} = 1$ shown on the right-middle is also similar except the interfacial region is even wider. The cases $k_{11} = 0.1, k_{22} = 1$; $k_{11} = 0.1, k_{22} = 10$ and $k_{11} = 1, k_{22} = 10$ are the analogous, with the roles of material 1 and 2 reversed.

The phase-field functional, the domain, and the boundary conditions have a symmetry, and we examine if the resulting designs reflect this symmetry. Specifically, note that if $\{u_1, u_2, \chi\}$ is a solution for a problem with k_1, k_2 on the square domain, then $\{1 - u_2, 1 - u_1, 1 - \chi\}$ is a solution for a problem with k_2, k_1 on the square domain obtained by changing x to $1 - x$. We see that our designs reflect this symmetry. Specifically, compare the case $k_{11} = 0.1, k_{22} = 1$ and the resulting design χ_1 shown in middle-left of Figure 3 and the case $k_{11} = 1, k_{22} = 0.1$ and the resulting design χ_2 shown in top-center of Figure 3. We see that $\chi_1(x, y) \approx 1 - \chi_2(1 - x, 1 - y)$.

Table 1 shows how the different contributions to the energy change for the various cases. It also shows how the flux varies. Further, it shows that the flux at the source, sink, and reaction zone all agree ensuring the "conversation of mass": species 1 is drawn in at the source, converted in the reaction and drawn out through the sink.

Figure 7 shows the designs for the same parameters, but for a volume fraction $v = 0.3$. The designs are similar, except the interface is more to the left.

3.2 Cylindrical reactor

Many reactors designed for thermochemical conversion devices implement a cylindrical ceramic structure that allow for even heating and easy transport of reactant gas. Thus, for the second example we look at an annular structure where the inner edge with $r = 0.2$ is held as the source

[1]We also study in the appendix the opposite case when $\alpha = \beta = 0$.

Table 1: Contributions to the energy functional $L(u, \chi)$, the phase field regularization, the flux J_i of each species calculated at the boundary, and the reaction integrated on the domain for $v = 0.5$.

k_{11}	k_{22}	Transport Energy $\int \frac{1}{2} \sum k_i \lvert\nabla u_i\rvert^2$	Reaction Energy $\int \frac{k_s}{2} \chi(1-\chi)(u_1-u_2)^2$	Phase Field	$J_{1,\text{in}}$ $\int k_1 \nabla u_1 \cdot \hat{n}$	$J_{2,\text{out}}$ $-\int k_2 \nabla u_2 \cdot \hat{n}$	Reaction $\int k_s \chi(1-\chi)(u_1-u_2)$
0.1	0.1	0.0451	0.0023	0.0203	0.0948	0.0948	0.0949
0.1	1	0.1706	0.0285	0.0748	0.3866	0.3977	0.3983
0.1	10	0.2952	0.2022	0.0779	0.9610	0.9947	0.9948
1	0.1	0.1706	0.0285	0.0550	0.3977	0.3864	0.3983
1	1	0.4276	0.0340	0.1070	0.9202	0.9201	0.9232
1	10	0.9044	0.3595	0.1502	2.5015	2.5256	2.5278
10	0.1	0.2953	0.2021	0.0574	0.9946	0.9602	0.9947
10	1	0.9044	0.3596	0.1150	2.5257	2.5011	2.5278
10	10	2.2730	0.9990	0.1699	6.5257	6.5254	6.5440

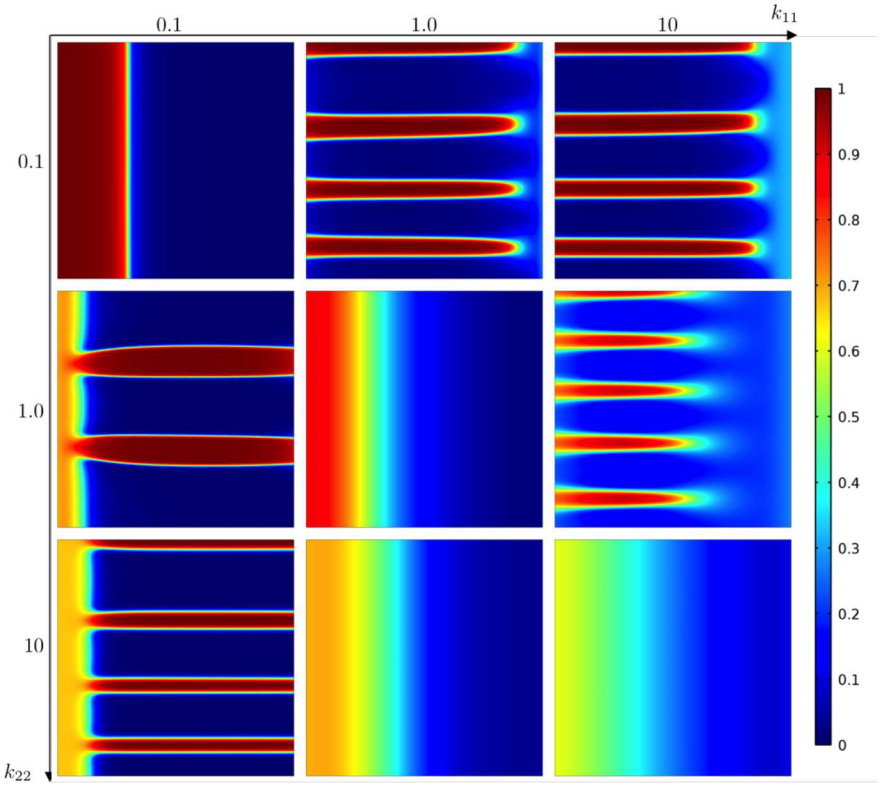

Figure 7: Parameter sweep with $v = 0.3$, $\alpha = 0.1$, $\beta = 5 \times 10^{-5}$, $k_{12} = 10^{-3} \times k_{11}$, $k_{21} = 10^{-3} \times k_{22}$, $k_s = 1 \times 10^2$.

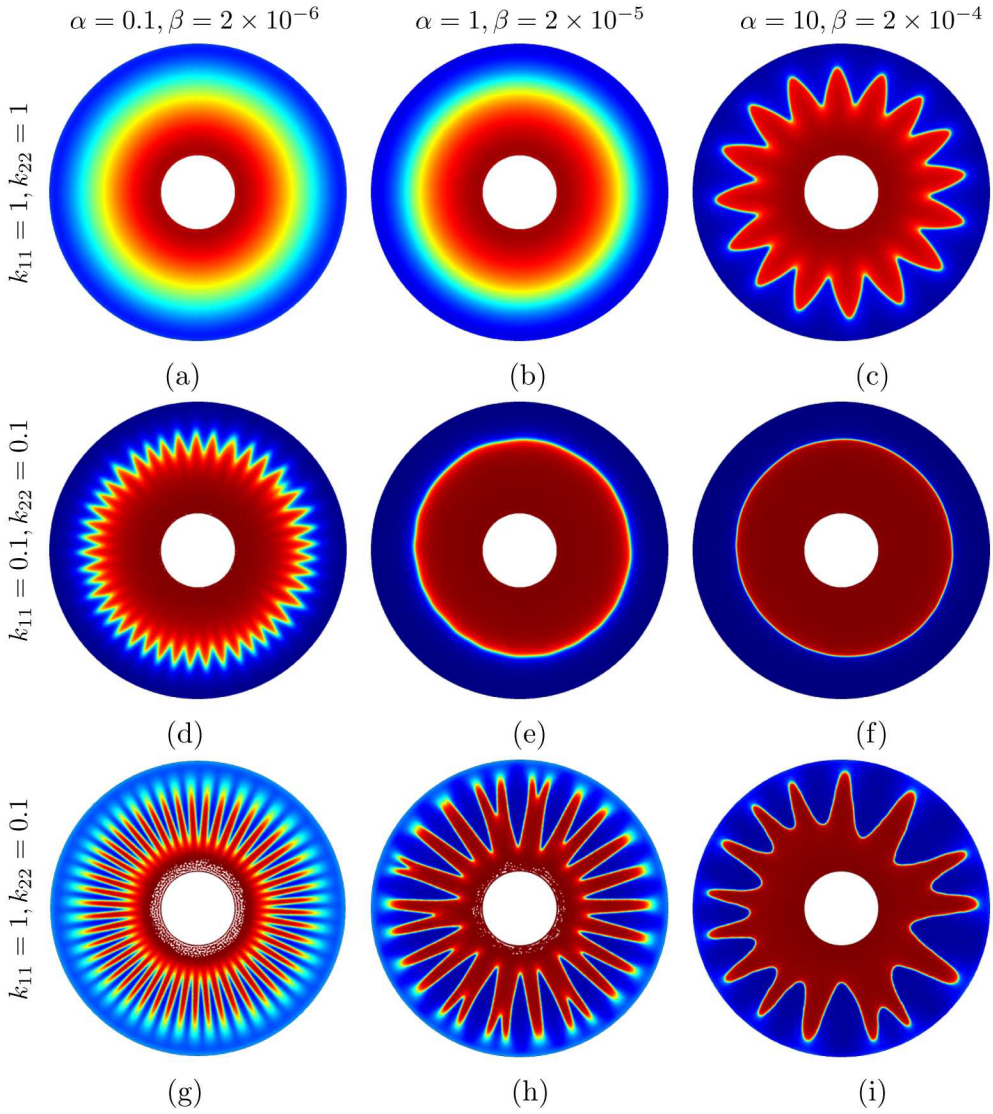

Figure 8: Designs for a cylindrical reactor with a source of the first species at the inner edge and a sink for the second species at the outer edge. The parameters are in (9) except as noted in the rows and columns of the figure. Further, $k_{12} = 10^{-2} \times k_{11}, k_{21} = 10^{-2} \times k_{22}$.

of the first chemical species ($\partial_1\Omega$ where $u_1 = 1$) and the outer at $r = 1$ is set as a sink for the second ($\partial_2\Omega$ where $u_2 = 0$). We consider the same parameters as (9). The resulting design is shown in Figure 8(b). The first species enters from the inside, reacts and converts to the second species which exits from the outside. Thus, we see much of the first material on the inside and the second on the outside. Further, to enable sufficient reaction, the interface region is diffuse. If we decrease the phase field coefficients by an order of magnitude, we obtain the design in Figure 8(a) where the mixed region increases as the penalty for deviating from the pure materials is reduced. On the other hand, increasing the phase field coefficients by an order of magnitude yields the design in Figure 8(c). Indeed, here, the penalty for deviation from the pure phases increases and therefore the interface becomes corrugated allowing sufficient reaction.

The second row of Figure 8 show the analogous result when the diffusivity is reduced by an order of magnitude. Transport is now harder compared to the reaction, and therefore nearly pure phases dominate to ensure transport to the interface. The interface is corrogated if the phase field coefficient is small but becomes smooth as it increases. The final row of Figure 8 shows the results for unequal conductivity. Since the transport of first species is easier, material 1 forms long arms to transport the first species to close to the outlet where the reaction takes place. Further, individually increasing the phase field parameters, α and β, promotes pure phases and leads to fewer arms, respectively.

3.3 Periodic cellular reactor

It is common to construct reactors as a periodic tubular array where the first species enters the reactor through one set of tubes while the second species is extracted from the reactor with a different set of tubes. Looking at a cross-section, one sees a square array of inlets and a square array of outlets. This motivates our next example where the reactor is taken to be periodic with the unit cell shown in Figure 9(a). The source is at the corners of the cell while the outlet is at the center. We look for a periodic design to optimize the transport as before. The resulting unit design for the parameters shown in (9) is shown in Figure 9(b). It is repeated periodically in Figure 9(c).

4 Conclusions

This paper aimed to examine numerical methods for designing optimal microstructures for energy conversion. We used a coupled, two-phase, reactive-diffusion system describing the transport of two chemical species each residing in separate phases (pore space and solid), and undergoing an interfacial conversion reaction. The optimal design problem associated with maximizing the through-put of the domain was numerically investigated using a phase field method, where intermediate densities are penalized to ensure manufacturability and an inherent length scale. Optimal interface shapes are dependent on transport parameters, but in general, saw-tooth or branched structures are obtained.

The simplified models provided a proof of concept and approach: with a full characterization of realistic transport and interfacial chemistry, the same method could be applied to design a real-world system. The reaction form prescribed at the interface could match stoichiometric ratios and mechanisms that were deduced experimentally. The relevant species to a real-world system could be tracked in a similar manner. Extensions of the transport models could include realistic fluid flow and interaction with the solid [7]. The optimal structures determined effectively yield designs with arbitrary length scales, and could be coupled well with additive manufacturing techniques to be experimentally verified. The "composite" regions or intermediate densities of the diffuse interface results can be interpreted as a separate length scale of porosity or material mixture.

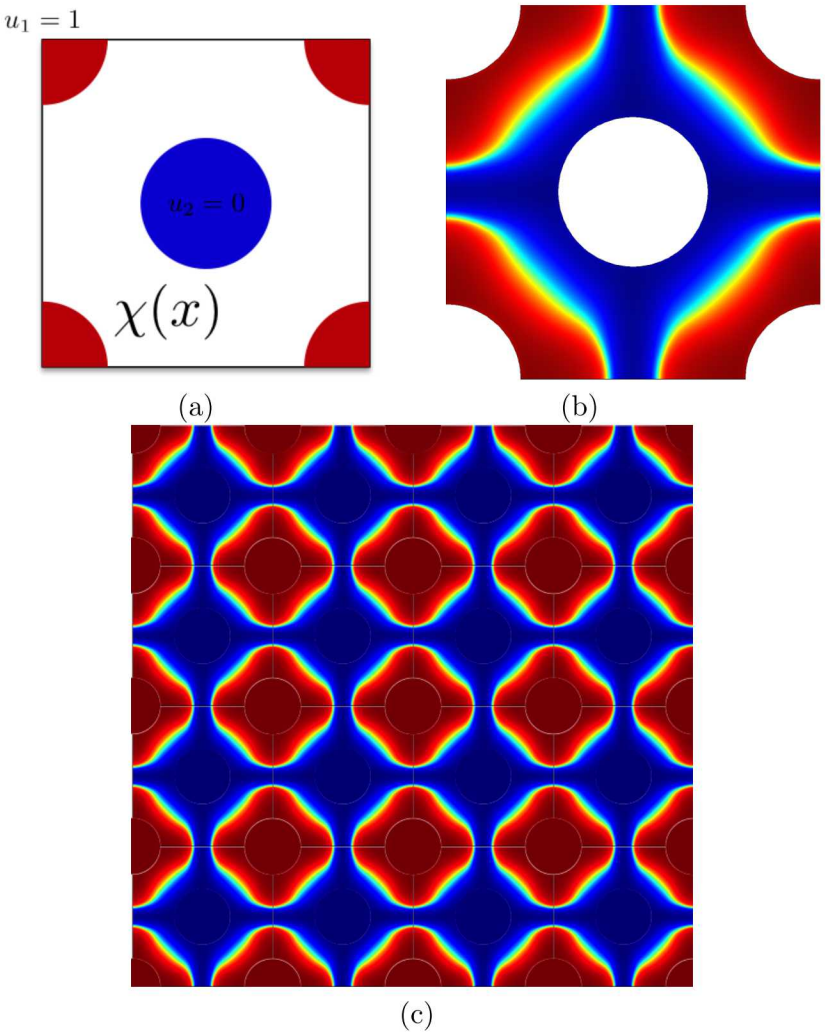

Figure 9: Periodic square distribution of circular sources and sinks. (a) Unit domain, (b) Resulting design on the unit domain, (c) Periodic design.

The construction of such a device would rely on being able to control this secondary porosity by the inclusion of space-filling material or other techniques. Regardless, the results found exemplify structures that balance interface area and two-phase transport.

Acknowledgement

This work draws from the doctoral thesis of LC at the California Institute of Technology. It is a pleasure to acknowledge many interesting discussions with Sossina M. Haile, Robert V. Kohn and Patrick Dondl. We gratefully acknowledge the financial support of the National Science Foundation through the PIRE grant: OISE-0967140.

Appendix

We have seen above that the optimal (phase field) design often involves oscillatory interfaces or a diffuse interface (which we argue is also an indication of oscillatory interfaces). To understand when such rough interfaces can occur, we study the problem without a phase field penalization:

$$O = \sup_{\chi\in\mathcal{X}} \inf_{u\in\mathcal{V}} \left\{ L(u,\chi) = \int_\Omega \frac{1}{2}\sum_{i=1,2} k_i|\nabla u_i|^2 + \frac{1}{2}\chi(1-\chi)u\cdot Au - \lambda\chi\, dx \right\}. \tag{10}$$

where $\lambda \in \mathbb{R}$ is given and

$$\mathcal{X} = L^2(\Omega;[0,1]) \quad \text{and} \quad \mathcal{V} = \{v \in H^1(\Omega;\mathbb{R}^2) : v_i = u_i^* \text{ on } \partial_i\Omega,\ i = 1,2\}.$$

We have the following explicit characterization of the optimal design problem (10).

Theorem 4.1. *We have*

$$O = \min_{v\in\mathcal{V}} \int_\Omega \overline{W}(v,\nabla v)\, dx.$$

where

$$\overline{W}(v,\xi) = \begin{cases} \frac{1}{2}\left(|\xi_1|^2 k_{21} + |\xi_2|^2 k_{22}\right) & (v,\xi)\in\mathcal{R}_0, \\ \dfrac{\left(\sum_i \Delta k_i|\xi_i|^2\right)^2 + 2\sum_i |\xi_i|^2(k_v(k_{i1}+k_{i2}) - 2\lambda\Delta k_i) + (k_v - 2\lambda)^2}{8k_v} & (v,\xi)\in\mathcal{R}, \\ \frac{1}{2}\left(|\xi_1|^2 k_{11} + |\xi_2|^2 k_{12} - 2\lambda\right) & (v,\xi)\in\mathcal{R}_1 \end{cases}$$

with

$$\begin{aligned} \mathcal{R}_0 &= \{(v,\xi) : \sum_i \Delta k_i|\xi_i|^2 - 2\lambda \le -k_v\}, \\ \mathcal{R} &= \{(v,\xi) : -k_v < \sum_i \Delta k_i|\xi_i|^2 - 2\lambda < k_v\}, \\ \mathcal{R}_1 &= \{(v,\xi) : \sum_i \Delta k_i|\xi_i|^2 - 2\lambda \ge k_v\}, \end{aligned}$$

and

$$\Delta k_i = k_{i1} - k_{i2}, \quad k_v = k_s(v_1 - v_2)^2.$$

This explicit characterization provides insights into when we see individual phases and when we see diffuse intermediate phases. The region $\mathcal{R}_0$ is where $\chi = 0$ and we have pure phase 2 while the region $\mathcal{R}_1$ is where $\chi = 1$ and we have pure phase 1. The region $\mathcal{R}$ is where we have $\chi \in (0,1)$ or the mixed phase region (which we interpret as fine scale structure). This region is shown as the shaded region in Figure 4 along with the contours of the function $\overline{W}$ for various parameters. Note that when $\lambda = 0$ and the two diffusivities and gradients are equal $k_{11} = k_{22}$, $|\xi_1| = |\xi_2|$ then we are in the mixed phase (or rough interface) regime. This is consistent with the numerical examples studied earlier.

Proof. For $v \in \mathbb{R}^2, \xi \in \mathbb{R}^{2\times 2}, \chi \in \mathbb{R}$, set

$$W(v,\xi,\chi) = \frac{1}{2}\sum_{i=1,2}(\chi k_{i1} + (1-\chi)k_{i2})|\xi_i|^2 + \frac{k_s}{2}\chi(1-\chi)v\cdot Av - \lambda\chi$$

and

$$\overline{W}(v,\xi) = \max_{\chi\in[0,1]} W(v,\xi,\chi). \tag{11}$$

Note that

$$O = \sup_{\chi\in\mathcal{X}}\inf_{v\in\mathcal{V}}\int_\Omega W(v,\nabla v,\chi)dx$$

We can show (see [13] for details) using Proposition 2.4 of Ekeland and Témam [17] that the saddle point problem is attained and the order can be reversed. Specifically, there exists $\bar{v} \in \mathcal{V}$, $\bar{\chi} \in \mathcal{X}$ such that

$$\begin{aligned} O &= \int_\Omega W(\bar{v},\nabla\bar{v},\bar{\chi})dx = \sup_{\chi\in\mathcal{X}}\inf_{v\in\mathcal{V}}\int_\Omega W(v,\nabla v,\chi)dx = \inf_{v\in\mathcal{V}}\sup_{\chi\in\mathcal{X}}\int_\Omega W(v,\nabla v,\chi)dx \\ &= \inf_{v\in\mathcal{V}}\int_\Omega \overline{W}(v,\nabla v)dx. \end{aligned}$$

It remains to compute $\overline{W}$. To that end, note that for a fixed v,ξ, $W(v,\xi,\chi)$ is quadratic in χ. Therefore, the equation

$$\frac{\partial W}{\partial\chi}(v,\xi,\chi) = 0$$

has an unique solution $\chi = \chi^*$. A simple calculation reveals

$$\chi^*(v,\xi) = \frac{\sum_i \Delta k_i|\xi_i|^2 + k_s(v_1-v_2)^2 - 2\lambda}{2k_s(v_1-v_2)^2}.$$

Notice that

$$\chi^*(v,\xi)\begin{cases} \le 0 & (v,\xi)\in\mathcal{R}_0, \\ \in(0,1) & (v,\xi)\in\mathcal{R}, \\ \ge 1 & (v,\xi)\in\mathcal{R}_1. \end{cases}$$

A longer, but straightforward, calculation reveals that

$$W(v,\xi,\chi^*) = \frac{\left(\sum_i \Delta k_i|\xi_i|^2\right)^2 + 2\sum_i(|\xi_i|^2 k_v(k_{i1}+k_{i2}) - 2\lambda\Delta k_i) + (k_v - 2\lambda)^2}{8k_v}.$$

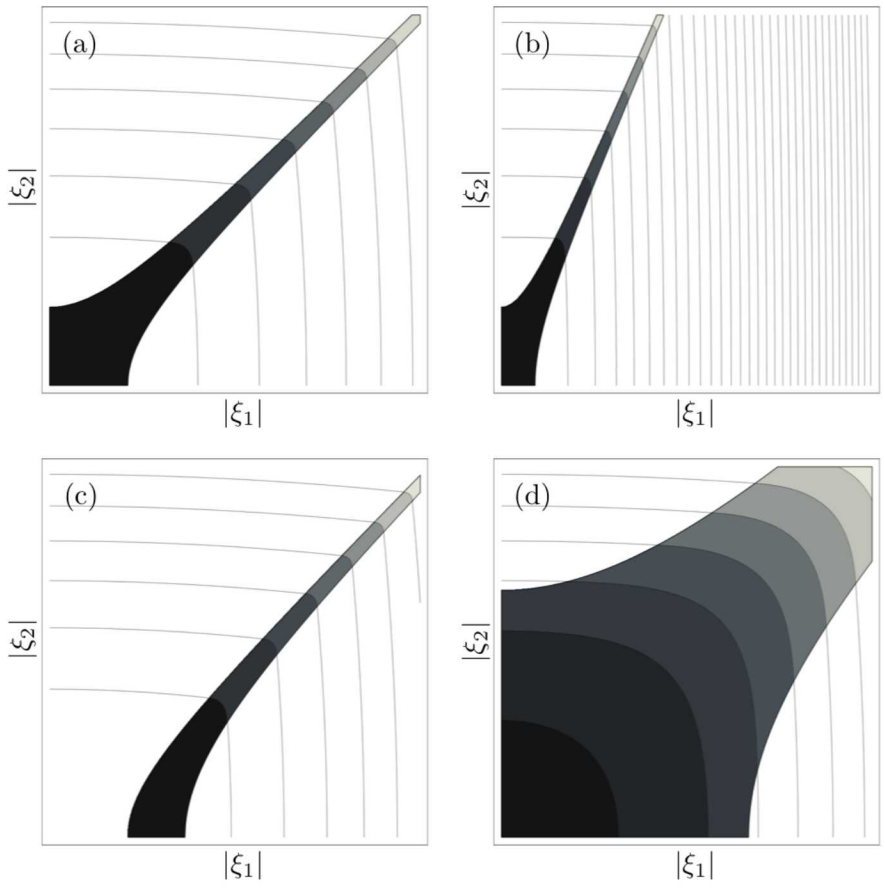

Figure 10: Contour plot of $\overline{W}$ for fixed v, λ. The shaded regions indicate where mixed phase ($\chi \in (0,1)$) occurs. (a) $k_{11} = k_{22} = k_s = 1, k_{12} = k_{21} = 0.1, (v_1 - v_2)^2 = 1, \lambda = 0$. (b) Parameters as in (a) except $k_{11} = 5$, (c) Parameters as in (a) except $\lambda = 1$, (d) Parameters as in (a) except $(v_1 - v_2)^2 = 10$.

Similarly,

$$W(v,\xi,0) = \frac{1}{2}\left(|\xi_1|^2 k_{21} + |\xi_2|^2 k_{22}\right),$$
$$W(v,\xi,1) = \frac{1}{2}\left(|\xi_1|^2 k_{11} + |\xi_2|^2 k_{12} - 2\lambda\right).$$

Now, we can verify by explicit calculation that

$$\begin{aligned} W(v,\xi,\chi^*) - W(v,\xi,0) &= \frac{k_v}{2}(\chi^*(v,\xi))^2 \\ W(v,\xi,\chi^*) - W(v,\xi,1) &= \frac{1}{4}(\chi^*(v,\xi) - 1)^2 \\ W(v,\xi,1) - W(v,\xi,0) &= \frac{1}{2}\left(\sum_i \Delta k_i |\xi_i|^2 - 2\lambda\right) \end{aligned} \tag{12}$$

We obtain the desired result by recalling (11), rewriting

$$\overline{W}(v,\xi) = \max\{\Psi(v,\xi)W(v,\xi,\chi^*), W(v,\xi,0), W(v,\xi,1)\}$$

where

$$\Psi(v,\xi) = \begin{cases} 1 & (v,\xi) \in \mathcal{R} \\ -\infty & else \end{cases}$$

and using (12).

□

References

[1] G. Allaire. *Shape Optimization by the Homogenization Method*. Applied Mathematical Sciences. Springer New York, 2001.

[2] Samuel M Allen and John W Cahn. A microscopic theory for antiphase boundary motion and its application to antiphase domain coarsening. *Acta Metallurgica*, 27(6):1085–1095, 1979.

[3] Luigi Ambrosio and Giuseppe Buttazzo. An optimal design problem with perimeter penalization. *Calculus of Variations and Partial Differential Equations*, 1(1):55–69, 1993.

[4] Antonino Salvatore Arico, Peter Bruce, Bruno Scrosati, Jean-Marie Tarascon, and Walter Van Schalkwijk. Nanostructured materials for advanced energy conversion and storage devices. *Nature materials*, 4(5):366–377, 2005.

[5] A. Atkinson, S. Barnett, R. J. Gorte, J. T. S. Irvine, A. J. McEvoy, M. Mogensen, S. C. Singhal, and J. Vohs. Advanced anodes for high-temperature fuel cells. *Nat Mater*, 3(1):17–27, 01 2004.

[6] M.P. Bendsoe and O. Sigmund. *Topology Optimization: Theory, Methods, and Applications*. Engineering online library. Springer Berlin Heidelberg, 2003.

[7] Thomas Borrvall and Joakim Petersson. Topology optimization of fluids in stokes flow. *International journal for numerical methods in fluids*, 41(1):77–107, 2003.

[8] Blaise Bourdin and Antonin Chambolle. Design-dependent loads in topology optimization. *ESAIM: Control, Optimisation and Calculus of Variations*, 9:19–48, 8 2003.

[9] Peter G Bruce, Bruno Scrosati, and Jean-Marie Tarascon. Nanomaterials for rechargeable lithium batteries. *Angewandte Chemie International Edition*, 47(16):2930–2946, 2008.

[10] Y-H Chen, C-W Wang, X Zhang, and Ann Marie Sastry. Porous cathode optimization for lithium cells: Ionic and electronic conductivity, capacity, and selection of materials. *Journal of Power Sources*, 195(9):2851–2862, 2010.

[11] William C. Chueh, Christoph Falter, Mandy Abbott, Danien Scipio, Philipp Furler, Sossina M. Haile, and Aldo Steinfeld. High-flux solar-driven thermochemical dissociation of CO_2 and H_2O using nonstoichiometric ceria. *Science*, 330(6012):1797–1801, 2010.

[12] Ryan MC Clemmer and Stephen Francis Corbin. Influence of porous composite microstructure on the processing and properties of solid oxide fuel cell anodes. *Solid State Ionics*, 166(3):251–259, 2004.

[13] Lincoln Nash Collins. *Optimal design of materials for energy conversion*. PhD thesis, California Institute of Technology, 2017.

[14] Comsol. *Multiphysics Reference Guide for COMSOL 5.1*, 2015.

[15] J Scott Cronin, James R Wilson, and Scott A Barnett. Impact of pore microstructure evolution on polarization resistance of Ni-Yttria-stabilized zirconia fuel cell anodes. *Journal of Power Sources*, 196(5):2640–2643, 2011.

[16] B. Dacorogna. *Direct Methods in the Calculus of Variations*. Applied Mathematical Sciences. Springer New York, 2007.

[17] I. Ekeland and R. Témam. *Convex Analysis and Variational Problems*. Society for Industrial and Applied Mathematics, 1999.

[18] J Goodman, R V Kohn, and L Reyna. Numerical study of a relaxed variational problem from optimal design. *Comput. Methods Appl. Mech. Eng.*, 57(1):107–127, August 1986.

[19] Y-S Hu, Philipp Adelhelm, Bernd M Smarsly, Sarmimala Hore, Markus Antonietti, and Joachim Maier. Synthesis of hierarchically porous carbon monoliths with highly ordered microstructure and their application in rechargeable lithium batteries with high-rate capability. *Advanced Functional Materials*, 17(12):1873–1878, 2007.

[20] Haiping Jia, Pengfei Gao, Jun Yang, Jiulin Wang, Yanna Nuli, and Zhi Yang. Novel three-dimensional mesoporous silicon for high power lithium-ion battery anode material. *Advanced Energy Materials*, 1(6):1036–1039, 2011.

[21] WooChul Jung, Julien O. Dereux, William C. Chueh, Yong Hao, and Sossina M. Haile. High electrode activity of nanostructured, columnar ceria films for solid oxide fuel cells. *Energy Environ. Sci.*, 5:8682–8689, 2012.

[22] Robert V. Kohn and Gilbert Strang. Optimal design and relaxation of variational problems, i. *Communications on Pure and Applied Mathematics*, 39(1):113–137, 1986.

[23] Yu Li, Zheng-Yi Fu, and Bao-Lian Su. Hierarchically structured porous materials for energy conversion and storage. *Advanced Functional Materials*, 22(22):4634–4667, 2012.

[24] Ole Sigmund and Kurt Maute. Topology optimization approaches. *Structural and Multidisciplinary Optimization*, 48(6):1031–1055, 2013.

[25] JR Smith, A Chen, D Gostovic, D Hickey, D Kundinger, KL Duncan, RT DeHoff, KS Jones, and ED Wachsman. Evaluation of the relationship between cathode microstructure and electrochemical behavior for SOFCs. *Solid State Ionics*, 180(1):90–98, 2009.

[26] David E Stephenson, Bryce C Walker, Cole B Skelton, Edward P Gorzkowski, David J Rowenhorst, and Dean R Wheeler. Modeling 3D microstructure and ion transport in porous Li-ion battery electrodes. *Journal of The Electrochemical Society*, 158(7):A781–A789, 2011.

[27] Toshio Suzuki, Zahir Hasan, Yoshihiro Funahashi, Toshiaki Yamaguchi, Yoshinobu Fujishiro, and Masanobu Awano. Impact of anode microstructure on solid oxide fuel cells. *Science*, 325(5942):852–855, 2009.

[28] Grant A. Umeda, William C. Chueh, Liam Noailles, Sossina M. Haile, and Bruce S. Dunn. Inverse opal ceria-zirconia: architectural engineering for heterogeneous catalysis. *Energy Environ. Sci.*, 1:484–486, 2008.

[29] Zhenhai Wen, Qiang Wang, Qian Zhang, and Jinghong Li. In situ growth of mesoporous SnO_2 on multiwalled carbon nanotubes: A novel composite with porous-tube structure as anode for lithium batteries. *Advanced Functional Materials*, 17(15):2772–2778, 2007.

[30] James R. Wilson, J. Scott Cronin, Anh T. Duong, Sherri Rukes, Hsun-Yi Chen, Katsuyo Thornton, Daniel R. Mumm, and Scott Barnett. Effect of composition of ($La_{0.8}Sr_{0.2}MnO_3$−Y_2O_3−stabilized ZrO_2) cathodes: Correlating three-dimensional microstructure and polarization resistance. *Journal of Power Sources*, 195(7):1829 – 1840, 2010.

[31] James R. Wilson, Worawarit Kobsiriphat, Roberto Mendoza, Hsun-Yi Chen, Jon M. Hiller, Dean J. Miller, Katsuyo Thornton, Peter W. Voorhees, Stuart B. Adler, and Scott A. Barnett. Three-dimensional reconstruction of a solid-oxide fuel-cell anode. *Nat Mater*, 5(7):541–544, 07 2006.